Kim et al. *NPG Asia Materials* (2021) 13:41
https://doi.org/10.1038/s41427-021-00305-z

NPG Asia Materials

ARTICLE Open Access

Metallic phase transition metal dichalcogenide quantum dots showing different optical charge excitation and decay pathways

Bo-Hyun Kim[1], Min-Ho Jang[2], Hyewon Yoon[3], Hyun Jun Kim[1], Yong-Hoon Cho[2], Seokwoo Jeon[3] and Sung-Ho Song[1]

Abstract

The charge excitation and decay pathways of two-dimensional heteroatomic quantum dots (QDs) are affected by the quantum confinement effect, bandgap structure and strong exciton binding energy. Recently, semiconducting transition metal dichalcogenides (TMDs) have been intensively studied; however, the charge dynamics of metallic phase QDs (*m*QDs) of TMDs remain relatively unknown. Herein, we investigate the photophysical properties of TMD-*m*QDs of two sizes, where the TMD-*m*QDs show different charge excitation and decay pathways that are mainly ascribed to the defect states and valence band splitting, resulting in a large Stokes shift and two excitation bands for maximum photoluminescence (PL). Interestingly, the dominant excitation band redshifts as the size increases, and the time-resolved PL peak redshifts at an excitation wavelength of 266 nm in the smaller QDs. Additionally, the lifetime is shortened in the larger QDs. From the structural and theoretical analysis, we discuss that the charge decay pathway in the smaller QDs is predominantly affected by edge oxidation, whereas the vacancies play an important role in the larger QDs.

Introduction

Following extensive studies on two-dimensional (2D) layered materials, transition metal dichalcogenide (TMD)-based quantum dots (QDs) have attracted significant attention owing to their potential applications in optoelectronics, catalysis, biosensors, energy systems, etc[1–4]. The different structural phases, i.e., semiconducting (2H) and metallic (1T/1T′) phases, of 2D TMDs with stoichiometric combinations (MX_2) of transition metals (M = Mo, W, Ni, etc.) and chalcogens (X = S, Se, Te) exhibit various electronic and optical properties[5–8]. The electronic and optical properties of TMD-QDs are usually explained by the combined mechanism of the quantum confinement effect, surface state, and doping effect[9–11], which is also sensitive to environmental conditions, chalcogen defects, and heteroatomic crystal structures[4,12,13]. As the QDs form a monolayer, the electronic band structure widens to ~3–5 eV, with slight variations depending on the type of transition metal and chalcogen[13,14]. Furthermore, TMD-QDs exhibit a strong exciton binding energy and significantly enhanced spin-valley coupling, which induces broadening of excitonic absorption peaks and generates a higher quantum yield compared to the flake types[2–4]. $MoSe_2$- and WS_2-QDs show an excitation wavelength-dependent photoluminescence (PL) shift, suggesting two different recombination pathways of excitons[15,16]. However, to date, the optical properties of metallic phase TMD-QDs (TMD-*m*QDs) compared to those of semiconducting TMD-QDs have been ambiguous and not consistently reported[4,17–19].

The spectroscopic results for metallic TMDs show additional Raman modes below 200 cm^{-1}, a monotonic

Correspondence: Seokwoo Jeon (jeon39@kaist.ac.kr) or Sung-Ho Song (shsong805@kongju.ac.kr)
[1]Division of Advanced Materials Engineering, Kongju National University, Chungnam 31080, South Korea
[2]Department of Physics and KI for the NanoCentury, KAIST, Daejeon 34141, South Korea
Full list of author information is available at the end of the article

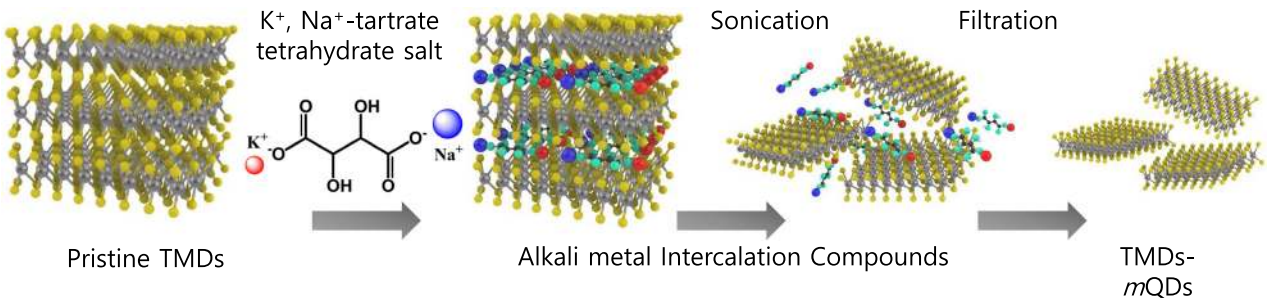

Fig. 1 Fabrication route for TMD-QDs. Schematic illustration of the synthetic process of TMDs-*m*QDs. The synthetic route is composed of three parts: forming compounds, making QDs, and filtering. Yellow and gray represent chalcogens and transition metals.

change in UV-visible absorption, and a shift in photoelectron peaks[6,20,21]. TMD-*m*QDs that are electrochemically, hydrothermally, or mechanically fabricated in situ with a structural phase transition have distinctive advantages, such as high charge transfer and efficient catalytic properties[4,22]. However, although the photophysical properties of metallic TMD-QDs are expected to be advantageous, most studies have focused on semiconducting TMD-QDs. This is mainly due to the various synthetic routes and particular phase engineering related to the metastable metallic phase of TMDs[6,7,21,23,24]. Phase engineering for metallic phase TMDs has been developed via methods such as intercalation of alkali metals, electron-beam irradiation, and plasmonic hot electron injection, among others, including direct synthesis[6,25,26]. Exfoliation by Li or K intercalation is the most preferred method for the synthesis of metallic phase TMDs[5,7,20,21], where high quality and phase stabilization are achieved simultaneously. Moreover, the phase stability is enhanced by lithiation, doping, vacancy defects, and lattice strain[7,21,27,28].

In this study, we report an in-depth investigation of the photophysical properties of metallic phase (1T/1T′) TMD (MX_2, M = Mo, W; X = S, Se)-QDs synthesized using the K and Na intercalation method, in which the TMD-*m*QDs were separated into two groups of different sizes (*m*QDs-I: ~3 nm, *m*QDs-II: ~12 nm). The metallic phase and structural properties were confirmed by high-resolution transmission electron microscopy (HR-TEM) showing an octahedral crystalline structure, novel Raman vibrational modes below 200 cm^{-1}, and redshifted X-ray photoelectron spectroscopy (XPS) spectra. For the photophysical properties, various spectroscopic methods were employed, including excitation-dependent PL (PLE) with two resonance excitation bands and peak shifted time-resolved PL (TRPL) spectroscopy. Density functional theory (DFT) calculations revealed that the oxidation defects at the edge structure and vacancies on the basal plane play a role in controlling the electronic structure and exciton dynamics. Based on these analyses, a photoelectronic model of TMD-*m*QDs is suggested.

Results

Synthesis and characterization

For years, we have developed the process of co-intercalation and exfoliation of TMDs using alkali metal-organic compounds, such as potassium sodium tartrate tetrahydrate salt, as shown in Fig. 1 (see details in the Experimental section and Supplementary Information)[5]. In this study, we adopt this method to synthesize metallic phase TMD (MoS_2, $MoSe_2$, WS_2, WSe_2)-QDs. The as-prepared TMD-salt compounds were instantly dispersed in water and sonicated for a few minutes, followed by filtration and dialysis. During the sonication process, TMD-QDs were explosively synthesized. Atomic force microscopy (AFM) and high-resolution transmission electron microscopy (HRTEM) revealed that the TMD-QDs separated into two groups have sizes of ~3 nm (QDs-I) and ~12 nm (QDs-II; Fig. 2a). The AFM measurement yielded a QD thickness of 1–2 nm, regardless of the lateral size, implying that most QDs are mono- or bilayers (Supplementary Fig. S1). Figure 2b shows digital photographs of QDs-I and QDs-II dispersed in water at a concentration of 0.1 mg/ml, where QDs-I are significantly brighter and closer to the blue color compared to QDs-II under UV illumination. The dispersion stability is longer than 1 month, which is attributed to the partially negatively charged QDs, as examined by the zeta potential (Supplementary Fig. S2). Furthermore, HRTEM images directly demonstrate the lateral size and circular structure of the QDs (Fig. 2c and Supplementary Fig. S3). The analysis of magnified HRTEM images (inset of Fig. 2c) shows that the lattice constants of the (100) plane are 0.25, 0.23, 0.2, and 0.24 nm for MoS_2, $MoSe_2$, WS_2, and WSe_2, respectively, which are slightly smaller than those reported for 2H semiconducting TMD layers[11,18,24,29]. The HRTEM image of QD-II shows point defects on the basal plane that are most likely related to chalcogen or metal atom vacancies (Fig. 2d, top)[1,30]. The corresponding fast Fourier transform pattern demonstrates the octahedral crystalline structure of QDs typically observed in metallic phase TMDs (Fig. 2d, bottom). The metallic

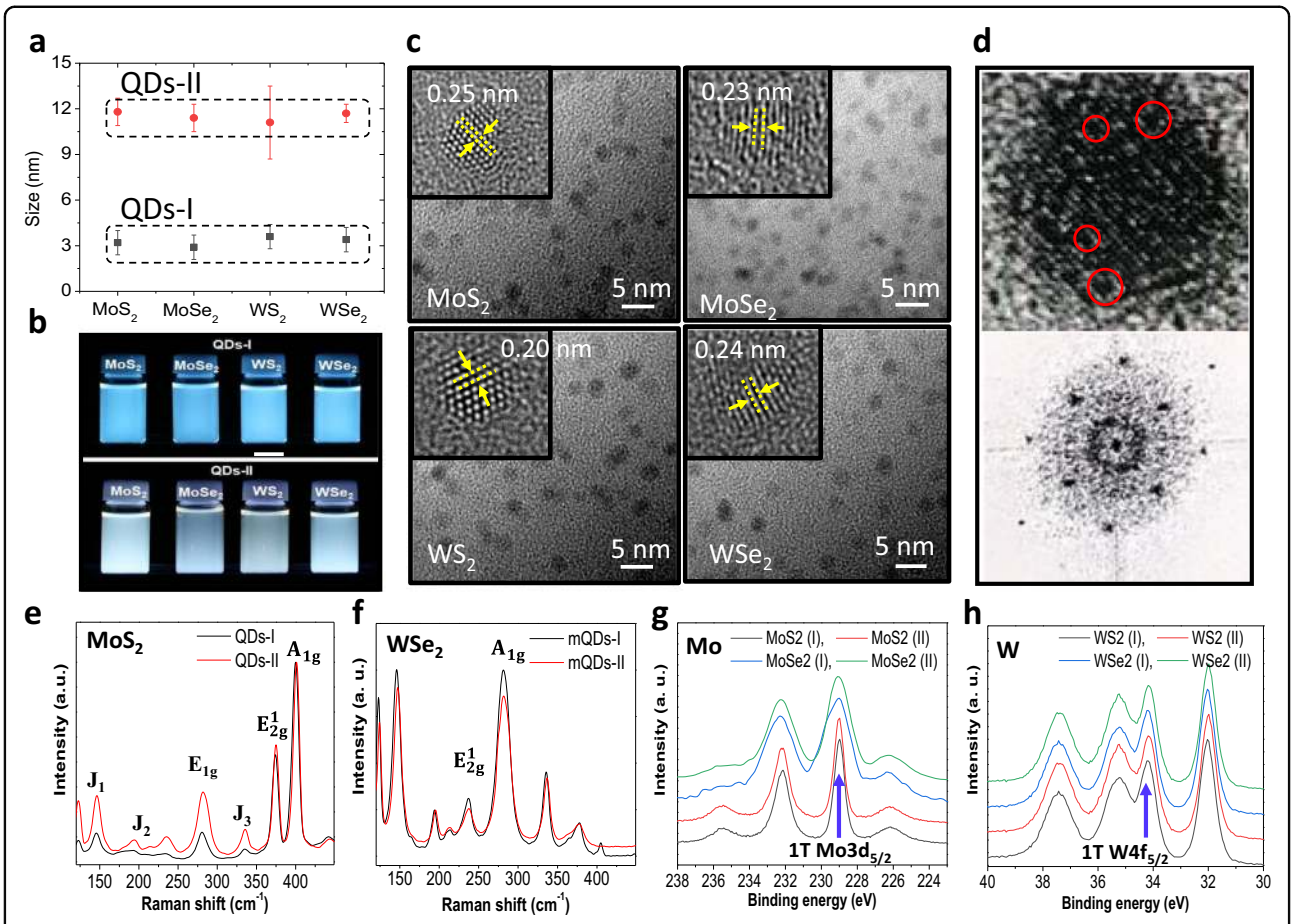

Fig. 2 Characterization of *m*QDs. a Size distribution of *m*QDs-I and *m*QDs-II. **b** Digital photographs of *m*QDs-I (top layer) and *m*QDs-II (bottom layer) dispersed in water at a concentration of 0.1 mg/ml. The pictures were taken under UV irradiation (255 nm). **c** TEM and HRTEM (inset) images of *m*QDs-I. The yellow dotted lines indicate the lattice constant of the (100) plane. **d** HRTEM image (top) and its fast Fourier transform pattern (bottom) of MoS_2 *m*QDs-II. The red circles indicate defects as vacancies on the basal plane of *m*QDs-II. **e**, **f** Raman signals of MoS_2 QDs (**e**) and WSe_2 QDs (**f**). **g**, **h** XPS spectra of Mo (**g**) and W (**h**). The blue arrows indicate the $Mo3d_{5/2}$ (**g**) and $W4f_{5/2}$ peaks observable from metallic Mo and W.

phase of the QDs is also complemented by Raman and XPS spectra (Fig. 2e, f and Supplementary Fig. S4a, b). Novel vibrational modes assigned to J_1 (146.5 cm^{-1}), J_2 (235 cm^{-1}), and J_3 (335.5 cm^{-1}) bands appear in both Raman spectra of MoS_2 QDs-I and QDs-II, which are indicative of the distinct Raman signature of metallic phase MoS_2 (Fig. 2e)[7,31]. Additionally, WSe_2 QDs show distinct vibrational modes below 225 cm^{-1} related to the J_1, J_2, and J_3 transitions, while the absence of a $B^1{}_{2g}$ peak at 304 cm^{-1} indicates a single layer similar to WSe_2 nanosheets (Fig. 2f)[24]. With the similar tendencies in all WS_2 and WSe_2-QDs[32,33], novel vibrational modes below 200 cm^{-1} are noted, suggesting that the as-prepared TMD-QDs are in the metallic phase (Fig. S4a, b). In the XPS spectra of the four different TMDs-QDs (Fig. 2g, h and Supplementary Fig. S4c, d), the transition metal and chalcogen peaks are shifted to lower binding energies and broadened with additional peaks compared to those of semiconducting 2H phase TMDs[18,34]. In the XPS spectra of Mo (Fig. 2g and Fig. S4c), the $Mo3d_{5/2}$ peak is shifted ~1 eV lower compared to that measured from 2H semiconducting MoX_2. In addition, separated W4f peaks clearly appear in the W spectra (Fig. 2h), and the assigned 1T $W4f_{5/2}$ peak is ~1 eV lower than the 2H $W4f_{5/2}$ peak (Fig. S4d). However, the characteristic in-plane $\left(E^1_{2g}\right)$ and/or out-of-plane (A_{1g}) vibrational modes in the Raman spectra and the peak shift of the metal atom to a lower binding energy in the XPS spectra indicate that the as-prepared TMD-QDs could contain some portion of the polymorph structure, although the metallic phases (1T/1T′) are still dominant.

Electronic and optical properties

The as-prepared TMD-*m*QDs-I and -*m*QDs-II were investigated by UV-visible (UV-vis) absorbance and PLE (i.e., excitation wavelength (λ_{Ex})-dependent emission wavelength (λ_{Em})) measurements to determine their

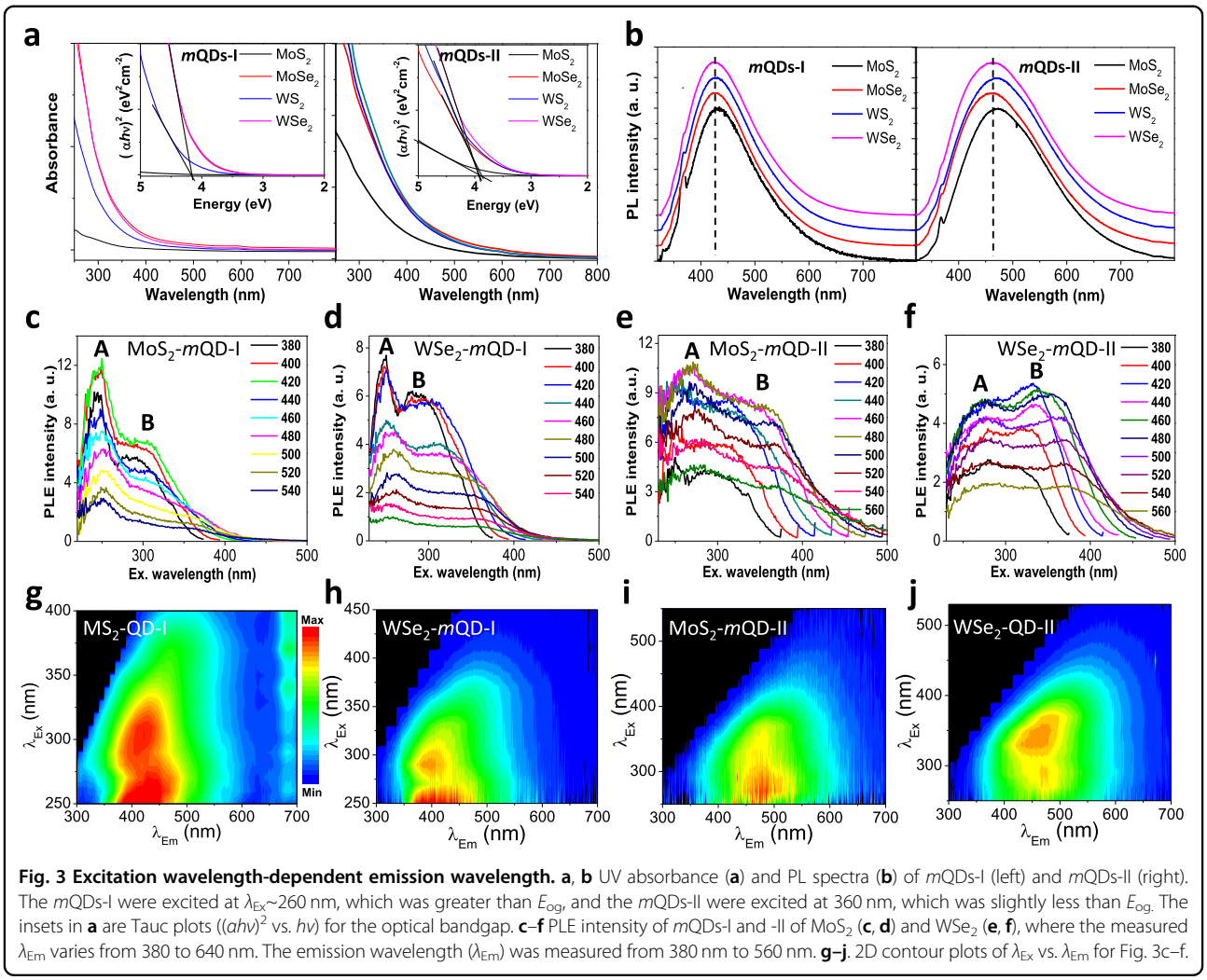

Fig. 3 Excitation wavelength-dependent emission wavelength. a, **b** UV absorbance (**a**) and PL spectra (**b**) of *m*QDs-I (left) and *m*QDs-II (right). The *m*QDs-I were excited at λ_{Ex}~260 nm, which was greater than E_{og}, and the *m*QDs-II were excited at 360 nm, which was slightly less than E_{og}. The insets in **a** are Tauc plots ($(\alpha h\nu)^2$ vs. $h\nu$) for the optical bandgap. **c**–**f** PLE intensity of *m*QDs-I and -II of MoS_2 (**c**, **d**) and WSe_2 (**e**, **f**), where the measured λ_{Em} varies from 380 to 640 nm. The emission wavelength (λ_{Em}) was measured from 380 nm to 560 nm. **g**–**j**. 2D contour plots of λ_{Ex} vs. λ_{Em} for Fig. 3c–f.

electronic and optical properties (Fig. 3). Figure 3a clearly shows monotonically decreasing UV-vis absorbance spectra in both *m*QDs-I (left) and *m*QDs-II (right), indicating the metallic properties of the QDs. The Tauc plot applied for the direct transition bandgap (E_{og}; inset of Fig. 3a) provides estimated values of $E_{og} = 4.14–4.20$ eV, except for $MoSe_2$, with values of ~3.85 eV in *m*QDs-I and 3.88–3.93 eV in *m*QDs-II, although there is a deviation depending on the stoichiometry of the TMDs. The E_{og} values larger than those of bulk or single-layer TMDs are assigned to an excitonic feature of the *m*QDs reflecting a strong quantum confinement effect[2,11,13,16], whereas the difference between *m*QDs-I and *m*QDs-II originates from the size difference. Figure 3b shows the PL spectra of *m*QDs-I excited at λ_{Ex} ~ 260 nm, which is $>E_{og}$, and those of *m*QDs-II excited at 360 nm, which is slightly $<E_{og}$. The spectral shapes are similar in each group but have different emission peaks (λ_{peak}) and linewidths (FWHM) (*m*QDs-I: $\lambda_{peak} = 427 \pm 3$ nm (2.90 eV), FWHM = 143 nm; *m*QDs-II: 464 ± 7 nm (2.67 eV), FWHM = 184 nm). The large Stokes shifts (~1.38 eV and ~0.78 eV) of the *m*QDs are noteworthy and ascribed to the large valance band splitting due to the strong spin-valley coupling, midgap state caused by defects, and enormously large exciton binding energy (>500 meV) in the *m*QDs in addition to vibrational relaxation and trion formation[18,35,36]. Figure 2c–f shows the PLE intensity of *m*QDs-I and -II of MoS_2 and WSe_2, where the measured λ_{Em} varies from 380 to 640 nm. Interestingly, in *m*QDs-I, two persistent intensity maximum peaks clearly appear at every λ_{Em} (Fig. 3c, d). The former is located at $\lambda_{Ex} = 240–260$ nm (A-band), and the latter is located at $\lambda_{Ex} = 290–375$ nm (B-band). These two excitation bands are consistently observed in another *m*QDs-I ($MoSe_2$ and WS_2, Supplementary Fig. S5a, b). The λ_{Ex} longer than 375 nm is related to the midgap states originating from defects[18]. The luminescence intensity peak in the A-band is independent of the stoichiometry of the TMDs for all measured λ_{Em}, whereas the B-band peak is redshifted and broadened as λ_{Em} increases. However, it is also weakly correlated with the stoichiometry

of the TMDs. This feature is consistently observed in *m*QDs-II, although the intensity peaks are broadened and move to the longer wavelength region (A-band: 260–285 nm, B-band: 310–390 nm; Fig. 3e, f and Supplementary Fig. S5c, d). Interestingly, in *m*QDs-I, the PL intensity peak in the A-band is higher than that in the B-band, whereas it is similar to or smaller than that in the B-band in *m*QDs-II. For example, in WSe_2 *m*QDs-II, the PL intensity in the A-band becomes like or smaller than that in the B-band (Fig. 3f). The two bands are certainly not related to the neutral free excitons or bound excitons of TMDs because of the monotonically decreasing UV absorption and single peak of the PL spectrum. This is probably due to the band splitting by strong spin-valley coupling and the quantum size effect because the ΔE between the two PLE peaks is ~0.7–0.9 eV, which is like the valence band splitting in semiconducting TMD-QDs[18]. To date, this feature has not been reported for semiconducting TMD-QDs, which will be discussed more later. Two-dimensional contour plots for the correlation between the excitation and emission wavelengths are shown in Fig. 3g–j and Supplementary Fig. S6e–h. Two regions of luminescence maximum intensity corresponding to the PLE spectra are evidently shown. The point of maximum intensity in *m*QDs-I oscillates slightly as λ_{Ex} increases from 250 to 340 nm, although it is gradually redshifted as λ_{Ex} increases beyond 300 nm, which is usually observed in QDs. In contrast, the oscillation propensity of *m*QDs-II is weakened, while the highest intensity area moves into the B-band region.

Exciton dynamics

To further investigate the exciton dynamics of the TMD-*m*QDs, TRPL measurements were performed at two λ_{Ex}. As shown in Fig. 4a, b, the TRPL spectra of WSe_2 *m*QDs-I at $\lambda_{Ex} = 266$ nm show that the PL peak gradually redshifts from ~410 to ~470 nm as the delay time increases, whereas in WSe_2 *m*QDs-II, the redshift of the PL peak is trivial even after a delay time of 30 ns. Quantitative analysis of the peak shift at $\lambda_{Ex} = 266$ nm reveals that while the peak of *m*QDs-I redshifts to above 200 meV, it is <100 meV in *m*QDs-II (Fig. 4e). In comparison, the peak shift of the TRPL spectra at $\lambda_{Ex} =$ 360 nm in both *m*QDs-I and -II is much less than that in WSe_2 *m*QDs-I excited at $\lambda_{Ex} = 266$ nm (Fig. 4c, d). The TRPL peak shift at $\lambda_{Ex} = 360$ nm is <100 meV in both *m*QDs-I and -II (Fig. 4f). This feature is analogously observed in all other TMD-*m*QDs (Supplementary Fig. S7). This suggests that some excitons formed at $\lambda_{Ex} =$ 266 nm on *m*QDs-I steadily transit to the lower energy states together with an emissive decay, whereas excitons formed at $\lambda_{Ex} = 360$ nm on *m*QDs-II are likely to predominantly decay at the occurring sites. This speculation is indirectly supported by the PL decay dynamics. Although all exciton decay profiles from *m*QDs-I and -II are best fitted by a multiexponential function, the profiles from *m*QDs-II are closer to the monoexponential decay line (Fig. 4g). The average PL lifetime of *m*QDs-I is 3.94 ± 0.12 ns at $\lambda_{Em} = 420$ nm, which is longer than the value of 2.98 ± 0.11 ns for *m*QDs-II at $\lambda_{Em} = 460$ nm (Fig. 4h and Supplementary Fig. S8). This indicates that the exciton decay dynamics are different between *m*QDs-I and -II, which can be ascribed to the different emission sites originating from different defects on the *m*QDs.

Theoretical calculation

To prove our speculation that the electronic structure is affected by defects on TMD-*m*QDs, first-principles calculations within the density functional theory (DFT) framework were performed on the representative structural model of MoS_2. Figure 5a shows the variation in the bandgap of MoS_2 *m*QDs without defects with the QD size, where the bandgap increases as the size decreases due to the quantum confinement effect. However, during the synthetic process, the formation of vacancy defects on the basal plane and oxidation of edge-exposed atoms are inevitable. Figure 5b schematically illustrates the chalcogen vacancy (top) and oxygen defect (bottom) of the MoS_2 structure. Structural defects are assumed based on XPS analysis (Supplementary Fig. S5). When considering such defects, the electronic bandgap of MoS_2 is narrower than that of the pristine structure (Fig. 5c). Unexpectedly, with the band structure calculations (Supplementary Fig. S9), the vacancy defect on the basal plane conspicuously leads to a bandgap narrowing up to 0.2–0.4 eV compared to that of pristine MoS_2, which is a significantly larger variation than that induced by oxygen defects on the edge structure (< 0.1 eV)[37]. Furthermore, the energy difference (0.2–0.3 eV) between them corresponds well to the difference (~0.3 eV) between the PL peaks of *m*QDs-I and *m*QDs-II (Fig. 3b).

Discussion

Herein, the photophysical properties of metallic phase TMD-QDs are reported by comparing *m*QDs-I (~3 nm) and *m*QDs-II (~12 nm) of two sizes. Based on the above results, a model for possible optical excitation and relaxation pathways in *m*QDs-I and *m*QDs-II is schematically illustrated in Fig. 6a, b. Because the ΔE (~0.8 eV) between two PLE excitation bands (Fig. 3c–f) corresponds well to that of valence band splitting in TMD-QDs[18], the system is assumed to be resonantly excited from the valence band splitting states to the conduction band (Sl and higher energy states) and lower defect states. Due to the metallic phase of QDs, strongly coupled exciton-plasmon polaritons might occur[38], where the resonance frequency varies with the size of *m*QDs. This, along with the defect-induced anisotropic confined excitons[12], may

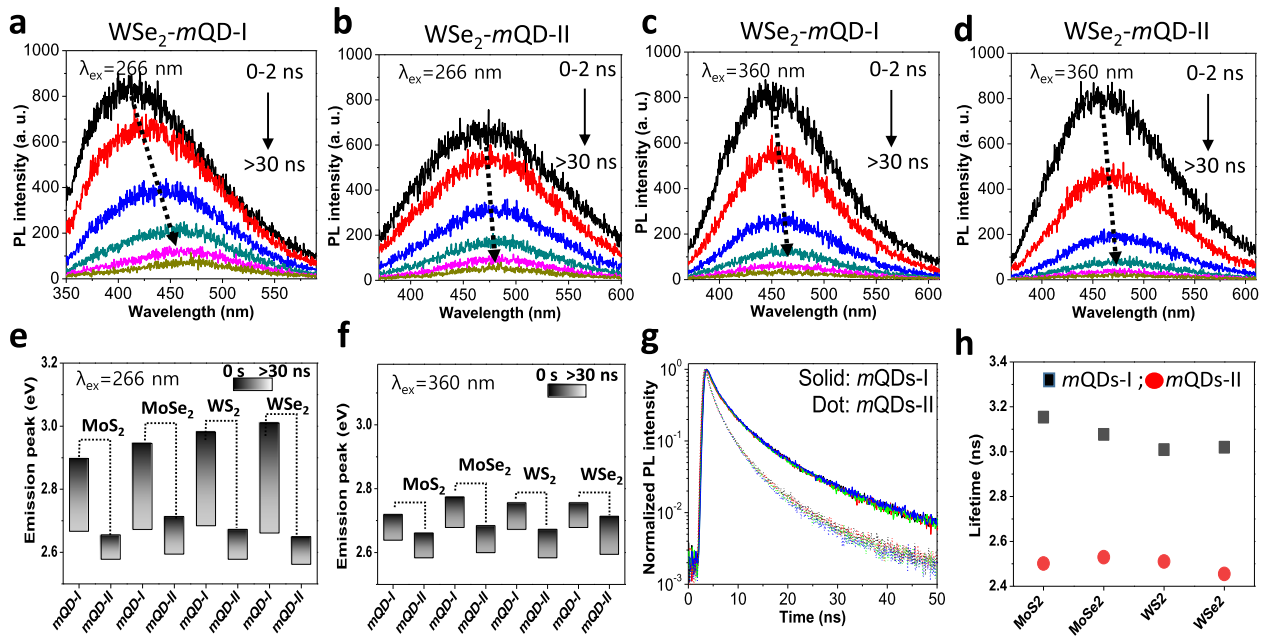

Fig. 4 Time-resolved photoluminescence (TRPL). a, **b** TRPL spectra with λ_{Ex} of 266 nm measured from WSe_2 *m*QDs-I (**a**) and *m*QDs-II (**b**). **c** Comparison of the PL peak shift between *m*QDs-I and *m*QDs-II based on Fig. 4a, b. **d**, **e** TRPL spectra with λ_{Ex} of 360 nm measured from WSe_2 *m*QDs-I (**d**) and *m*QDs-II (**e**). **f** Comparison of the PL peak shift between *m*QDs-I and *m*QDs-II based on Fig. 4d, e. Each PL intensity is accumulated for 0–2, 2–6, 6–12, 12–20, 20–30, and >30 ns. **g** Time-resolved PL decay profile. Solid-line is for mQDs-I at λEm = 420 nm and dots is for mQDs-II at λEm = 460 nm. **h** Average PL lifetimes of mQDs-I and mQDs-II calculated from Fig. 3g.

cause oscillation of the PLE intensity peak (Fig. 3g–j) and variation of the relative quantum efficiency in *m*QDs-I and *m*QDs-II after considering UV absorption (Supplementary Fig. S10). Additionally, as the edge oxidation of *m*QDs-I with a size comparable to the exciton Bohr radius has a dominant effect on the electronic structure (Fig. 6a), which is in contrast to *m*QDs-II mainly affected by vacancy defects (Fig. 6b), the radiative decay site of excitons is different from that in *m*QDs-II, which results in the difference in the energy (~0.3 eV) and lifetime (~1 ns) of PL. This is supported by structural analysis (Fig. 2 and Supplementary Figs. S3–5) and theoretical DFT calculations (Fig. 5). In addition, the vacancy and edge oxidation defects inducing substantial electron density localization cause a large Stokes shift (Fig. 3b)[35].

In summary, the electronic and optical properties of metallic phase TMD-QDs (*m*QDs) revealed that the exciton quantum dynamics are affected by the quantum confinement effect, band splitting due to strong spin-valley coupling, and defects. Two resonance excitation bands and oscillation of the PLE intensity peak of TMD-*m*QDs are first reported, which have not yet been reported in semiconducting TMD-QDs. When the size of *m*QDs is close to the exciton Bohr radius, edge oxidation has a dominant effect on the electronic structure; however, if the size is sufficiently larger than the exciton Bohr radius, then the vacancy on the basal plane acts as the main site determining the electronic structure and exciton dynamics. Our findings expand the general understanding of the nonlinear photophysics of two-dimensional heteroatomic structured QDs, which is essential for the potential applications of excitons-plasmons induced by light-matter interactions in optoelectronics and bio-optoelectronics.

Materials and methods

Metallic phase TMD-QDs

Potassium sodium tartrate was used to intercalate Li and K into the TMDs at low temperature. The metal-intercalated compounds of TMDs were reacted in the autoclave vessel at 250 °C for 12 h and then instantly exfoliated in water with sonication. The synthesized mQDs were separated into two sizes through filtration and dialysis5.

Characterization

The morphology of *m*QDs was analyzed using AFM (SPA400, SII, Japan) in tapping mode under ambient conditions. UV/Vis spectra (UV-3101PC spectrometer), fluorescence spectra (Perkin-Elmer LS 55 luminescence spectrometer), XPS (Sigma Probe, AlKα), and transmission electron microscopy (TEM, Tiatan cubed G2 60-300) analyses were conducted. Raman spectra were obtained from 100 to 500 cm^{-1} using a Raman spectrometer (LabRAM HR

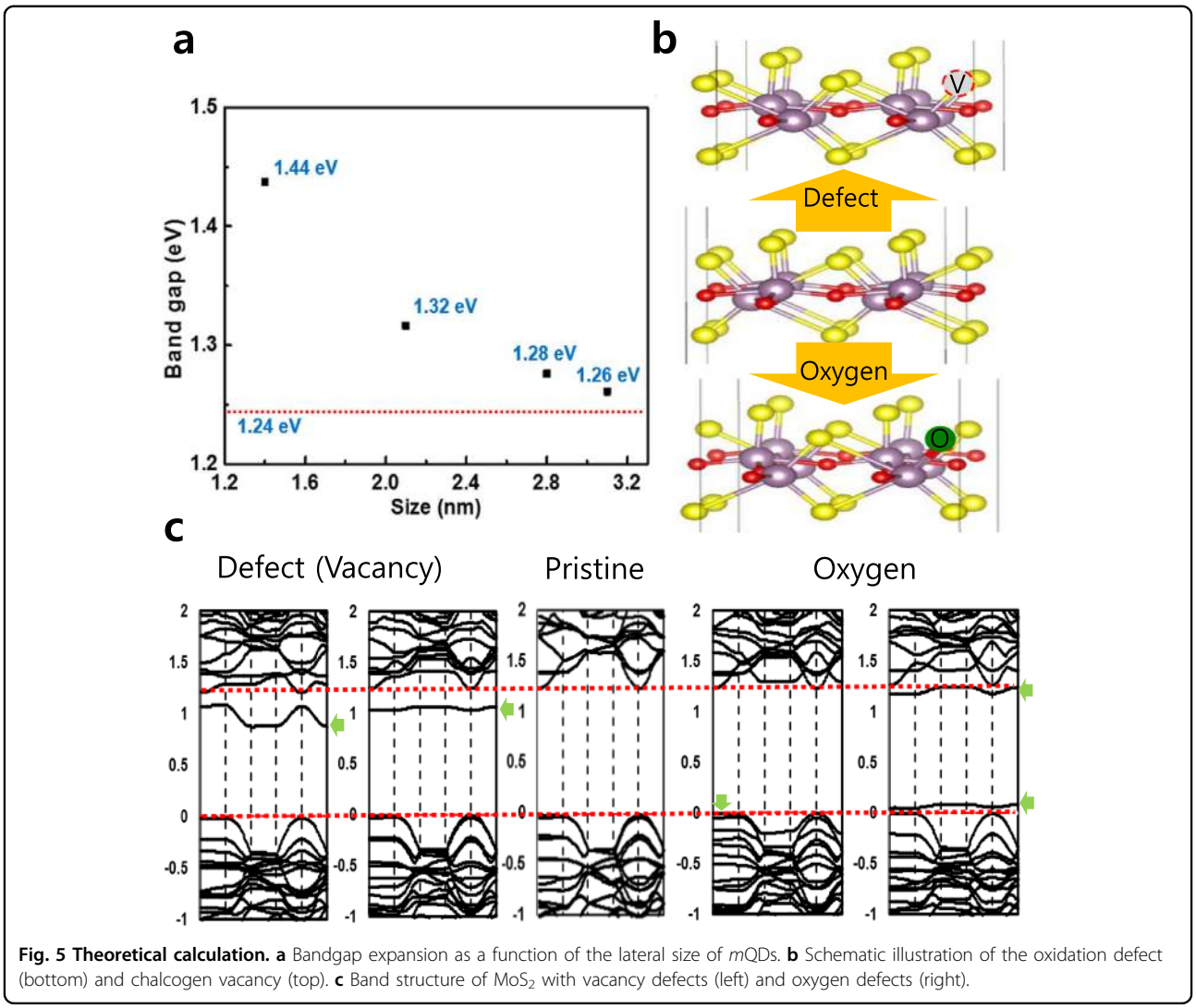

Fig. 5 Theoretical calculation. a Bandgap expansion as a function of the lateral size of *m*QDs. **b** Schematic illustration of the oxidation defect (bottom) and chalcogen vacancy (top). **c** Band structure of MoS_2 with vacancy defects (left) and oxygen defects (right).

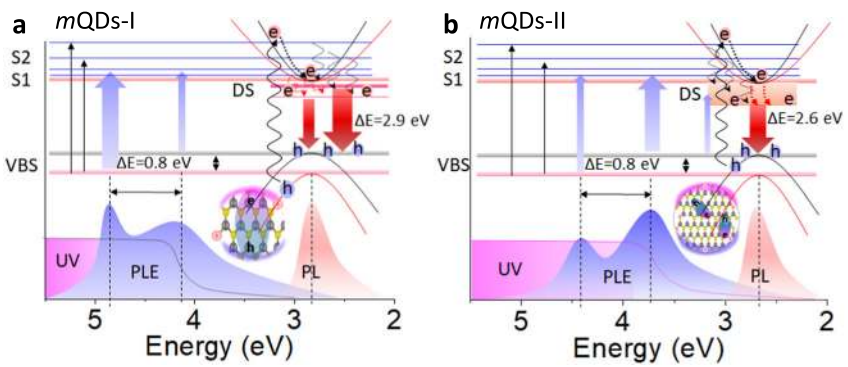

Fig. 6 Model for photophysical properties. Energy band diagram combined with UV absorption, PLE, and PL spectra of *m*QDs-I (**a**) and *m*QDs-II (**b**).

UV/Vis/NIR, excitation at 514 nm). PL measurements were carried out using a 325-nm He-Cd continuous-wave laser, monochromatic light from a 300W Xenon lamp, and UV spectrometers (Maya2000, Ocean Optics, USA) as a PL detector at room temperature.

Density functional calculations

DFT calculations were performed using the generalized gradient approximation (GGA) for the exchange-correlation potential and projector augmented wave potentials, as implemented in the VASP code. The wave functions were expanded in plane waves up to an energy cutoff of 400 eV. We employed a supercell geometry with a vacuum region of more than 8 Å to prohibit interactions between adjacent supercells (more details are given in the Supplementary Information).

Acknowledgements
This research was supported by the Basic Science Research Program through the National Research Foundation of Korea (NRF) funded by the Ministry of Education (2019R1A6A1A03032988). Additionally, this research was supported by the Basic Science Research Program through the National Research Foundation of Korea (NRF) founded by the Ministry of Education (NRF-2020R1I1A307162812, NRF-2020R1I1A01073220). M.H.J. and Y.-H.C. were supported by the National Research Foundation (NRF-2020M3E4A1080112) of the Korean government.

Author details
[1]Division of Advanced Materials Engineering, Kongju National University, Chungnam 31080, South Korea. [2]Department of Physics and KI for the NanoCentury, KAIST, Daejeon 34141, South Korea. [3]Department of Materials Science and Engineering, Graphene Research Center of KI for the NanoCentury, KAIST, Daejeon 34141, South Korea

Author contributions
B.H.K., S.J., and S.-H.S. proposed and conducted the overall project, and M.H.J. and Y.-H.C. carried out the TRPL experiments. H.W.Y. and S.J. developed the synthetic process of MQDs. B.H.K. and S.-H.S. analyzed the data and composed the manuscript.

Data availability
The authors declare that all data supporting the findings of this study are available within the paper and its supplementary information file.

Conflict of interest
The authors declare no competing interests.

Supplementary information The online version contains supplementary material available at https://doi.org/10.1038/s41427-021-00305-z.

Received: 3 December 2020 Revised: 26 January 2021 Accepted: 19 February 2021.
Published online: 23 April 2021

References

1. Ding, X. et al. Defect engineered bioactive transition metals dichalcogenides quantum dots. *Nat. Commun.* **10**, 1–13 (2019).
2. Wang, X., Sun, G., Li, N. & Chen, P. Quantum dots derived from two-dimensional materials and their applications for catalysis and energy. *Chem. Soc. Rev.* **45**, 2239–2262 (2016).
3. Xu, Y., Wang, X., Zhang, W. L., Lv, F. & Guo, S. Recent progress in two-dimensional inorganic quantum dots. *Chem. Soc. Rev.* **47**, 586–625 (2018).
4. Xu, Q. et al. Two-dimensional quantum dots: Fundamentals, photoluminescence mechanism and their energy and environmental applications. *Mater. Today Energy* **10**, 222–240 (2018).
5. Song, S. H. et al. Bandgap widening of phase quilted, 2D MoS2 by oxidative intercalation. *Adv. Mater.* **27**, 3152–3158 (2015).
6. Voiry, D., Mohite, A. & Chhowalla, M. Phase engineering of transition metal dichalcogenides. *Chem. Soc. Rev.* **44**, 2702–2712 (2015).
7. Tan, S. J. et al. Chemical stabilization of 1T′ phase transition metal dichalcogenides with giant optical Kerr nonlinearity. *J. Am. Chem. Soc.* **139**, 2504–2511 (2017).
8. Huang, H., Fan, X., Singh, D. J. & Zheng, W. T. Recent progress of TMD nanomaterials: phase transitions and applications. *Nanoscale* **12**, 1247–1268 (2020).
9. Park, N.-M., Choi, C.-J., Seong, T.-Y. & Park, S.-J. Quantum confinement in amorphous silicon quantum dots embedded in silicon nitride. *Phys. Rev. Lett.* **86**, 1355 (2001).
10. Zhu, S. et al. The photoluminescence mechanism in carbon dots (graphene quantum dots, carbon nanodots, and polymer dots): current state and future perspective. *Nano Res.* **8**, 355–381 (2015).
11. Gan, Z. et al. Quantum confinement effects across two-dimensional planes in MoS2 quantum dots. *Appl. Phys. Lett.* **106**, 233113 (2015).
12. Srivastava, A. et al. Optically active quantum dots in monolayer WSe 2. *Nat. Nanotechnol.* **10**, 491 (2015).
13. Lin, L. et al. Fabrication of luminescent monolayered tungsten dichalcogenides quantum dots with giant spin-valley coupling. *ACS Nano* **7**, 8214–8223 (2013).
14. Xiao, D., Liu, G.-B., Feng, W., Xu, X. & Yao, W. Coupled spin and valley physics in monolayers of MoS 2 and other group-VI dichalcogenides. *Phys. Rev. Lett.* **108**, 196802 (2012).
15. Caigas, S. P. et al. Origins of excitation-wavelength-dependent photoluminescence in WS2 quantum dots. *Appl. Phys. Lett.* **112**, 092106 (2018).
16. Luan, C.-Y. et al. Elucidation of luminescent mechanisms of size-controllable MoSe2 quantum dots. *Appl. Phys. Lett.* **111**, 073105 (2017).
17. Bayat, A. & Saievar-Iranizad, E. Synthesis of blue photoluminescent WS2 quantum dots via ultrasonic cavitation. *J. Lumin.* **185**, 236–240 (2017).
18. Zhang, K. et al. Ultrasmall and monolayered tungsten dichalcogenide quantum dots with giant spin–valley coupling and purple luminescence. *ACS Omega* **3**, 12188–12194 (2018).
19. Jin, H. et al. Colloidal single-layer quantum dots with lateral confinement effects on 2D exciton. *J. Am. Chem. Soc.* **138**, 13253–13259 (2016).
20. Park, S., et al. Phase engineering of transition metal dichalcogenides with unprecedentedly high phase purity, stability, and scalability via molten-metal-assisted intercalation. *Adv. Mater.* **32**, 2001889 (2020).
21. Chen, W. et al. Quantum dots of 1T phase transitional metal dichalcogenides generated via electrochemical Li intercalation. *ACS Nano***12**, 308–316 (2018).
22. Tan, C. et al. Preparation of high-percentage 1T-phase transition metal dichalcogenide nanodots for electrochemical hydrogen evolution. *Adv. Mater.* **30**, 1705509 (2018).
23. Lin, Y.-C., Dumcenco, D. O., Huang, Y.-S. & Suenaga, K. Atomic mechanism of the semiconducting-to-metallic phase transition in single-layered MoS 2. *Nat. Nanotechnol.* **9**, 391–396 (2014).
24. Sokolikova, M. S., Sherrell, P. C., Palczynski, P., Bemmer, V. L. & Mattevi, C. Direct solution-phase synthesis of 1T'WSe 2 nanosheets. *Nat. Commun.* **10**, 1–8 (2019).
25. Kang, Y. et al. Plasmonic hot electron induced structural phase transition in a MoS2 monolayer. *Adv. Mater.* **26**, 6467–6471 (2014).
26. Friedman, A. L. et al. Evidence for chemical vapor induced 2H to 1T phase transition in MoX 2 (X= Se, S) transition metal dichalcogenide films. *Sci. Rep.* **7**, 1–9 (2017).
27. Tang, Q. Tuning the phase stability of Mo-based TMD monolayers through coupled vacancy defects and lattice strain. *J. Mater. Chem. C* **6**, 9561–9568 (2018).
28. Shang, B. et al. Lattice-mismatch-induced ultrastable 1T-phase MoS2–Pd/Au for plasmon-enhanced hydrogen evolution. *Nano Lett.* **19**, 2758–2764 (2019).

29. Dai, T.-J. et al. Synthesis of few-layer 2H-MoSe2 thin films with wafer-level homogeneity for high-performance photodetector. *Nanophotonics* **7**, 1959–1969 (2018).
30. Carozo, V. et al. Optical identification of sulfur vacancies: Bound excitons at the edges of monolayer tungsten disulfide. *Sci. Adv.* **3**, e1602813 (2017).
31. Liu, L. et al. Phase-selective synthesis of 1T′ MoS 2 monolayers and heterophase bilayers. *Nat. Mater.* **17**, 1108–1114 (2018).
32. Pierucci, D. et al. Evidence for a narrow band gap phase in 1T′ WS2 nanosheet. *Appl. Phys. Lett.* **115**, 032102 (2019).
33. Yin, Y. et al. Synergistic phase and disorder engineering in 1T-MoSe2 nanosheets for enhanced hydrogen-evolution reaction. *Adv. Mater.* **29**, 1700311 (2017).
34. Rohaizad, N., Mayorga-Martinez, C. C., Sofer, Z. K. & Pumera, M. 1T-phase transition metal dichalcogenides (MoS2, MoSe2, WS2, and WSe2) with fast heterogeneous electron transfer: application on second-generation enzyme-based biosensor. *ACS Appl. Mater. Interfaces* **9**, 40697–40706 (2017).
35. Liu, Y., Kim, D., Morris, O. P., Zhitomirsky, D. & Grossman, J. C. Origins of the stokes shift in PbS quantum dots: impact of polydispersity, ligands, and defects. *ACS Nano* **12**, 2838–2845 (2018).
36. Fan, P. et al. Trion-induced distinct transient behavior and stokes shift in WS2 monolayers. *J. Phys. Chem. Lett.* **10**, 3763–3772 (2019).
37. Jeong, T. Y. et al. Spectroscopic studies of atomic defects and bandgap renormalization in semiconducting monolayer transition metal dichalcogenides. *Nat. Commun.* **10**, 1–10 (2019).
38. Van Tuan, D., Scharf, B., Žutić, I. & Dery, H. Marrying excitons and plasmons in monolayer transition-metal dichalcogenides. *Phys. Rev. X* **7**, 041040 (2017).